

PAPER • OPEN ACCESS

## High performance 4.7 THz GaAs quantum cascade lasers based on four quantum wells

To cite this article: Keita Ohtani *et al* 2016 *New J. Phys.* **18** 123004

View the [article online](#) for updates and enhancements.

### You may also like

- [Surface science motivated by heating of trapped ions from the quantum ground state](#)  
Dustin A Hite, Kyle McKay and David P Pappas
- [A single-laser scheme for observation of linear Breit-Wheeler electron-positron pair creation](#)  
Yutong He, I-Lin Yeh, T G Blackburn *et al.*
- [An integral-free representation of the Dyson series using divided differences](#)  
Amir Kalev and Itay Hen

### Recent citations

- [Terahertz Intersubband Electroluminescence from Nonpolar m-Plane ZnO Quantum Cascade Structures](#)  
Bo Meng *et al*
- [Six-level hybrid extraction/injection scheme terahertz quantum cascade laser with suppressed thermally activated carrier leakage](#)  
Boyu Wen *et al*
- [Anisotropic magnetic properties of excitons in GaAs multiple quantum wells](#)  
S. Haldar *et al*



## OPEN ACCESS

RECEIVED  
8 June 2016REVISED  
20 October 2016ACCEPTED FOR PUBLICATION  
10 November 2016PUBLISHED  
2 December 2016Original content from this  
work may be used under  
the terms of the [Creative  
Commons Attribution 3.0  
licence](#).Any further distribution of  
this work must maintain  
attribution to the  
author(s) and the title of  
the work, journal citation  
and DOI.

## PAPER

## High performance 4.7 THz GaAs quantum cascade lasers based on four quantum wells

Keita Ohtani<sup>1,3</sup>, Dana Turčinková<sup>1</sup>, Christopher Bonzon<sup>1</sup>, Ileana-Cristina Benea-Chelmus<sup>1</sup>, Mattias Beck<sup>1</sup>, Jérôme Faist<sup>1</sup>, Matthias Justen<sup>2</sup>, Urs U Graf<sup>2</sup>, Marc Mertens<sup>2</sup> and Jürgen Stutzki<sup>2</sup><sup>1</sup> Institute for Quantum Electronics, ETH Zurich, Auguste-Piccard-Hof 1, 8093 Zurich, Switzerland<sup>2</sup> KOSMA, 1. Physikalisches Institut, Universität zu Köln, D-50937 Köln, Germany<sup>3</sup> Author to whom any correspondence should be addressed.E-mail: [otanik@phys.ethz.ch](mailto:otanik@phys.ethz.ch)**Keywords:** quantum cascade laser, THz, GaAs/AlGaAs

## Abstract

GaAs/AlGaAs quantum cascade lasers based on four quantum well structures operating at 4.7 THz are reported. A large current density dynamic range is observed, leading to a maximum operation temperature of 150 K for the double metal waveguide device and a high peak output power more than 200 mW for the single surface plasmon waveguide device. A continuous wave, single mode, third order distributed feedback laser with a low electrical power dissipation and a narrow far-field beam pattern, which is required for a local oscillator in astronomy heterodyne spectrometers, is also demonstrated.

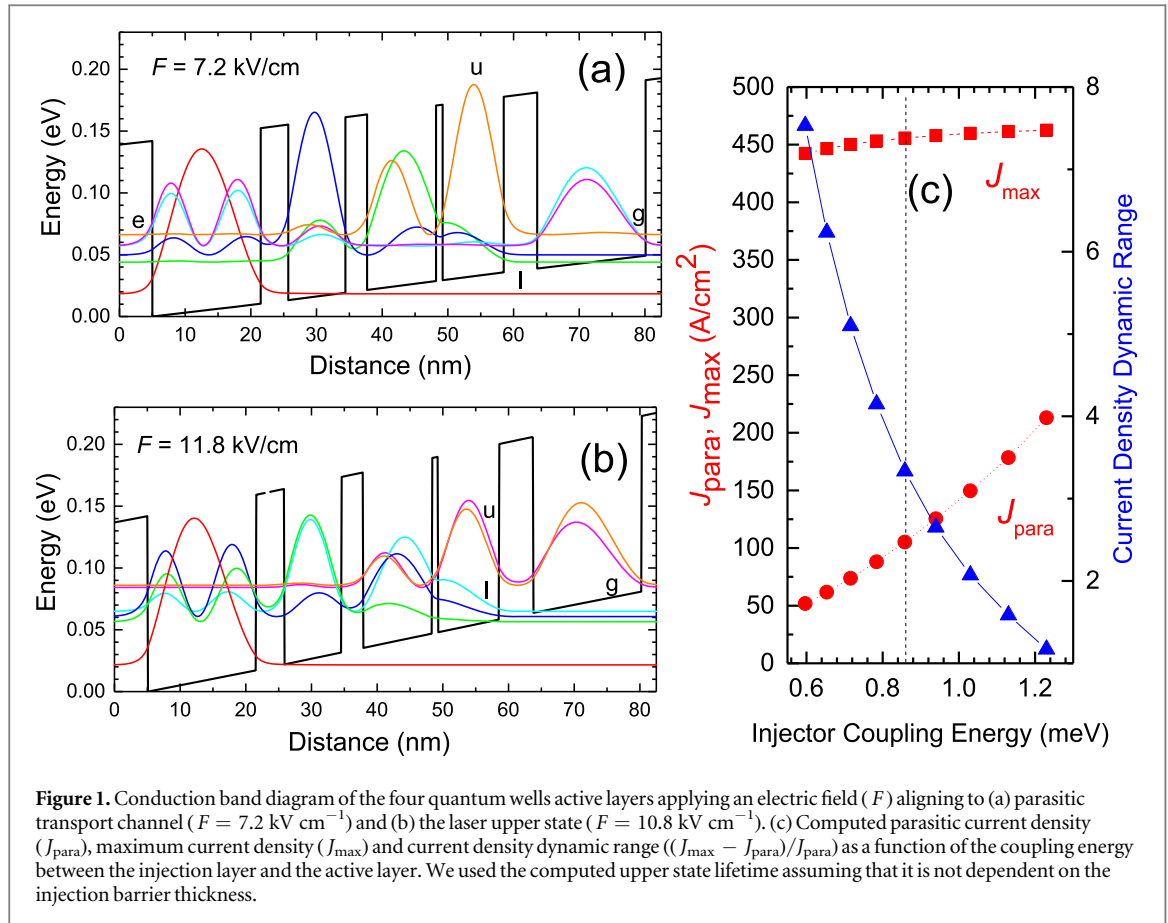
Quantum cascade lasers (QCLs) are unipolar semiconductor lasers using carrier recycling in the active region [1]. Making use of intersubband transitions in quantum wells (QWs) enables us to design a large optical gain coefficient covering a wide spectral range. In addition, unique waveguide structures make it possible to lase in the terahertz (THz) spectral region [2–4], leading to novel spectroscopic applications such as a chemical remote sensing and imaging [5, 6].

As demonstrated [7, 8], THz QCL is especially a good candidate to be used as a local oscillator in THz heterodyne spectrometer, that is a powerful tool for radio astronomy that studies space and planetary objects by detecting various spectral lines. There are several important spectral lines in THz region for astronomical observation: for example, the CII fine structure line at 1.9 THz, and the OH fine structure line at 1.8, 2.5, and 3.5 THz [9]. In particular, the fine structure line of the neutral atomic oxygen at 4.745 THz is of great interest since it is an important cooling line in the interstellar medium that relates to star bursts [9–11]. Compared to other existing THz coherent sources such as a gas laser, THz QCL combines high output power, high spectral purity, spectral tunability, low electrical power dissipation and compactness, which are highly required for usage in airborne platform laboratory. In the operation frequency range of the state-of-art THz QCLs, 4.745 THz is close to the highest operation frequency of these devices (5.4 THz) [12]. Unlike around 3 THz where QCL performance peaks and a number of studies have been reported [13], there are few reports in the higher frequency region [10, 12, 14, 15]. Here we exploit THz QCLs operating around 4.6–4.8 THz for application to local oscillators in the heterodyne spectrometer.

It has been generally accepted that the laser performance of high frequency THz QCLs is limited by a non-radiative energy relaxation via a thermally activated longitudinal optical (LO) phonon scattering whereas a parasitic current is the source for limited performance of the low frequency THz QCLs, resulting in a sweet spot operation frequency around 3 THz [13, 16]. A thermally activated LO phonon scattering time ( $\tau$ ) for electrons in the laser upper state is expressed as

$$\tau^{-1} = \tau_{LO}^{-1} \exp((E_{LO} - E_{ul})/k_B T_e), \quad (1)$$

where  $E_{LO}$  is the LO phonon energy,  $E_{ul}$  is the energy spacing between the laser upper and lower states,  $T_e$  is the electron temperature of the laser upper state, and  $\tau_{LO}$  represents the LO phonon scattering time for the electrons with kinetic energy of  $E_{LO} - E_{ul}$  [16, 17]. For higher frequency THz QCLs, the laser upper state lifetime



exponentially decreases at elevated temperature because thermally activated electrons tend to emit an LO phonon because of the smaller energy ( $= E_{\text{LO}} - E_{\text{ul}}$ ) difference between  $E_{\text{LO}}$  ( $\approx 36 \text{ meV}$  for GaAs) and  $E_{\text{ul}}$  ( $\approx 20 \text{ meV}$ ). Hence threshold current density ( $J_{\text{th}}$ ) rapidly increases, resulting in a lower characteristics temperature ( $T_0$ ) of  $J_{\text{th}}$ . When  $J_{\text{th}}$  exceeds the maximum current density ( $J_{\text{max}}$ ), laser action ceases by decreasing the injection efficiency due to formation of electric field domain boundaries. As a consequence, the maximum operation temperature ( $T_{\text{max}}$ ) would be lower because the current density dynamic range defined as  $(J_{\text{max}} - J_{\text{th}})/J_{\text{th}}$  significantly decreases with temperature.

For improvement upon it, we take a simple approach to increase the current density dynamic range of THz QCLs: a four QW structure based on GaAs/ $\text{Al}_{0.15}\text{Ga}_{0.85}\text{As}$  material, where one QW is bridged between the active QWs and the electron extraction QW, is employed because it exhibits an inherently smaller parasitic current ( $J_{\text{para}}$ ) [18].  $J_{\text{para}}$  is attributed to the wavefunction coupling between the ground state (denoted by 'g' in figure 1(a)) in the electron extraction QW and the excited state ('e' in figure 1(a)) of the adjacent electron extraction QW in the next period. Because it occurs before pumping the laser upper state,  $J_{\text{para}}$  provides a minimum of  $J_{\text{th}}$ . Since the bridged QW spatially separates the active QWs and the electron extraction QW,  $J_{\text{para}}$  would be expected to decrease due to their smaller wavefunction coupling. For the four QWs structure, the injection barrier thickness is an important parameter to increase the current density dynamic range since it determines  $J_{\text{max}}$  and  $J_{\text{para}}$ . Although a thinner injection barrier increases  $J_{\text{max}}$ ,  $J_{\text{para}}$  also becomes large enough to limit  $J_{\text{th}}$  because of the short lifetime ( $\approx 0.25 \text{ ps}$ ) of the excited state in the electron extraction QW. Figure 1(c) shows the computed  $J_{\text{max}}$ ,  $J_{\text{para}}$  and current density dynamic range as a function of coupling energy when the ground state in the electron extraction QW is aligned with the laser upper state as depicted in figure 1(b). The Kazarinov—Suris model [19, 20] was here used with an assumption that  $J_{\text{th}}$  is limited by  $J_{\text{para}}$ . We also used the computed upper state lifetime ( $= 5 \text{ ps}$ ) neglecting a radiative current and assumed that the in-plane electron momentum scattering time is  $1 \text{ ps}$  [21]. The normalized oscillator strength of the laser transition ( $f' = 0.67$ ) was selected since a high selective carrier injection into the laser upper state would be possible for a large  $E_{\text{ul}}$ . Although employing a thinner injection barrier increases  $J_{\text{max}}$ , it leads to a smaller current density dynamic range since  $J_{\text{para}}$  also increases rapidly with the coupling energy. In this work the injection barrier thickness ( $5.1 \text{ nm}$ ) with a coupling energy ( $\hbar\Omega$ ) of  $0.85 \text{ meV}$  is selected keeping  $J_{\text{max}}$  large for a higher output power together with a large current density dynamic range. The designed emission energy is  $19.2 \text{ meV}$ . Starting from the injection barrier, the layer thickness in nanometer is **5.1/9.3/1.0/10.5/3.3/8.7/4.2/16.5**, where GaAs layers are in roman font,  $\text{Al}_{0.15}\text{Ga}_{0.85}\text{As}$  are in bold, and the silicon doped layer ( $n = 2.0 \times 10^{16} \text{ cm}^{-3}$ ) is underlined.

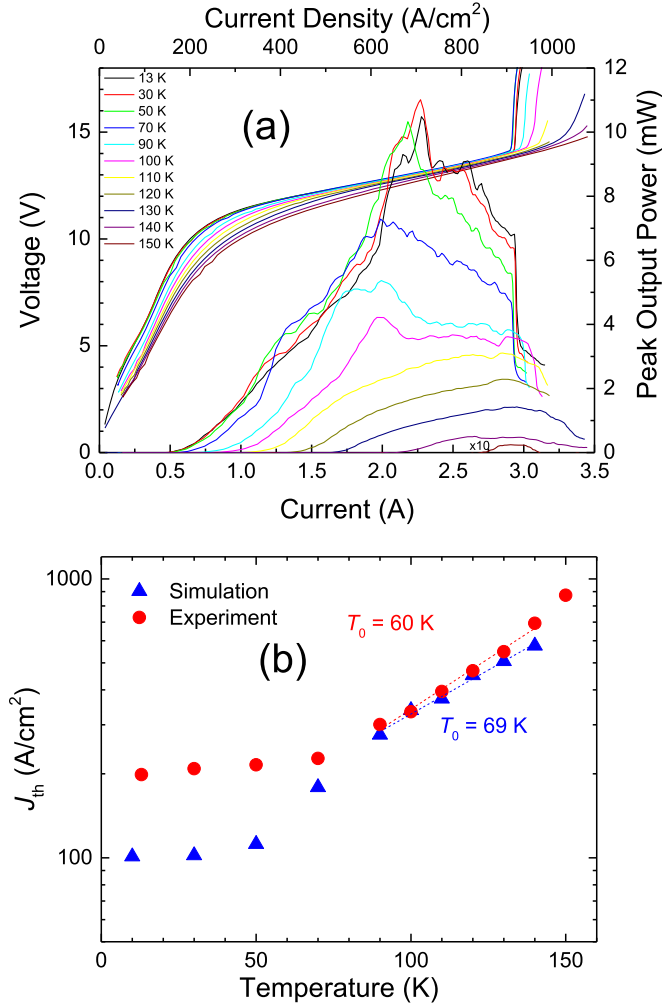


**Figure 2.** (a) Temperature dependent light output–current–voltage characteristics of the Cu double metal waveguide ridge laser. A helium cooled Si bolometer was used for light detection. The maximum operation temperature was 150 K. (b) Threshold current density ( $J_{th}$ ) as a function of temperature. Red circles represent  $J_{th}$  from the experiment while blue triangles denote the simulated one by the DM model. By fitting  $J_{th}$  in the range from 90 to 140 K,  $T_0$  ( $= 60$  K for the experiment and 69 K for the simulation) were obtained.

The laser structure was grown on Si-GaAs (001) substrate by solid-source MBE. The laser structure started with a 200 nm thick  $Al_{0.5}Ga_{0.5}As$  etching stop layer, followed by a 400 nm thick  $n$ -GaAs bottom contact layer ( $n = 3.0 \times 10^{18} \text{ cm}^{-3}$ ). Then 200 periods of GaAs/AlGaAs four QW active region (total thickness: 11.7  $\mu\text{m}$ ) was grown. At the end, a 40 nm thick  $n$ -GaAs top contact layer ( $n = 3.8 \times 10^{18} \text{ cm}^{-3}$ ) and a 20 nm thick  $n$ -InGaAs cap layer ( $n = 1.0 \times 10^{19} \text{ cm}^{-3}$ ) was grown on top of the active region. X-ray diffraction spectra show that the measured period thickness is in good agreement to the design. The MBE grown wafers were then processed into ridge laser structures with a double metal waveguide or a single surface plasmon waveguide. For a double metal waveguide, in order to decrease the waveguide losses, the bottom  $n$ -GaAs contact layer was etched away after removing the GaAs substrate. The processed wafers were cleaved into laser devices with ridge widths of 160  $\mu\text{m}$  and cavity lengths of 1.0–3.0 mm. The optical power measurements were carried out by the Thomas Keating Ltd THz power meter. The power meter was placed in front of the cryostat window as close as possible without any collection optics because of the large surface of the detector element. Also we did not correct for the transmission of the polymethylpentene cryostat window.

Figure 2(a) shows temperature dependent light ( $L$ )–current ( $I$ )–voltage ( $V$ ) characteristics of the Cu–Cu double metal waveguide device with a cavity length of 2.0 mm. Current started flowing by subband alignment between the ground state in the electron extraction QW and the lower states of the laser transition. Lasing started with  $J_{th} = 200 \text{ A cm}^{-2}$  right after pumping the parasitic transport channel ( $V = 7\text{--}9$  V).  $J_{max}$  reached  $920 \text{ A cm}^{-2}$  where the negative differential resistance voltage appeared at  $V = 14.2$  V, which is in close agreement with the designed one ( $V = 13.8$  V). The device provided a large current density dynamic range of 3.6, which is significantly larger than previously reported at high frequency THz QCLs ( $\approx 1$  for 4.4 THz QCL [22] and  $\approx 2$  for 4.7 THz and 5.4 THz QCLs [12, 15]). The maximum output peak power ( $P$ ) was 11 mW with the

slope efficiency of  $7 \text{ mW A}^{-1}$  at 10 K.  $T_{\text{max}}$  was 150 K, which, to our knowledge, is the highest operation temperature for higher frequency THz QCLs [23]. The device equipped with the Au–Au double metal waveguide with a ridge width of  $160 \text{ }\mu\text{m}$  and a cavity length of  $2.25 \text{ mm}$  long exhibited similar  $L$ – $I$ – $V$  characteristics with lower  $T_{\text{max}}$  ( $=142 \text{ K}$ ) (not shown).

Figure 2(b) depicts  $J_{\text{th}}$  as a function of temperature. Fitting data from 90 to 140 K via the empirical equation ( $J_{\text{th}} = J_0 \exp(T/T_0)$ ) expressing  $T_0$  of  $J_{\text{th}}$  results in  $T_0 = 60 \text{ K}$ , which is lower than the value of  $T_0$  (80 K) of the 3 THz QCLs [18] based on the same four QW scheme. As derived from equation (1), this is due to the larger thermally activated laser upper state lifetime originated from the smaller  $E_{\text{LO}} - E_{\text{ul}}$ . To evaluate  $T_0$ , we computed temperature dependence of  $J_{\text{th}}$  by the density matrix (DM) model taking into account of the kinetic energy balance for electrons [24]. In this model, electron-impurity scattering, interface roughness scattering, and alloy disorder scattering are included as an elastic scattering mechanism. The electron temperature ( $T_e$ ) is defined as an averaged electron temperature over all subbands in one period of the active region. Here the total loss ( $= \alpha_w + \alpha_m$ , where  $\alpha_m$  is mirror loss and  $\alpha_w$  is waveguide loss) is assumed to be  $30 \text{ cm}^{-1}$  [25] which is independent on temperature. Also the electron extraction is supposed to be done not by resonant tunneling but by resonant LO phonon scattering.  $T_0 = 69 \text{ K}$  obtained by simulated  $J_{\text{th}}$  from 90 to 140 K is in close agreement with the experimental value ( $= 60 \text{ K}$ ). In addition, the simulated  $J_{\text{th}}$  shows a weak temperature dependence in the temperature range from 10 to 50 K comparable to the experimental  $J_{\text{th}}$ ; the computed  $T_e$  is almost constant ( $\approx 50 \text{ K}$ ) until the lattice temperature reaches 50 K, thus suppressing to exponentially decrease the upper state lifetime as shown in equation (1) if  $T_e$  increases with the lattice temperature. Thus those facts imply that our DM model predicts right  $T_e$  and reproduces thermally activated carrier scattering processes in the active region. However, it underestimates the absolute value of  $J_{\text{th}}$  by a factor of two in this temperature range most probably due to underestimation of the elastic scattering rate. This leads to the larger simulated current density dynamic range ( $= 5.1$ ) compared to the experimental one ( $= 3.6$ ).

In addition to the observed  $T_{\text{max}}$ , a remarkable feature of the large current density dynamic range is the capability of high  $P$  when a large out-coupling waveguide such as a single surface plasmon waveguide is employed. Figure 3(a) shows  $L$ – $I$ – $V$  curves of the device equipped with a single surface plasmon waveguide. The device had  $150 \text{ }\mu\text{m}$  wide ridge and  $1.0 \text{ mm}$  long cavity. Current pulses of  $75 \text{ ns}$  width with a repetition frequency of  $10 \text{ kHz}$  were used. One of the facets was high-reflection coated by  $\text{Al}_2\text{O}_3$  ( $200 \text{ nm}$ )/Au ( $100 \text{ nm}$ ) films.  $I$ – $V$  characteristics exhibited the same current density dynamic range ( $\approx 3.6$ ) as that of the double metal waveguide.  $J_{\text{th}}$  was  $300 \text{ A cm}^{-2}$  at 10 K. As expected, the device delivered  $P = 220 \text{ mW}$  at 10 K, which is among the highest peak power so far obtained from the same device size [22, 26]. Moreover, as depicted in figure 3(b), another device having  $200 \text{ }\mu\text{m}$  wide and  $6.5 \text{ mm}$  long, with uncoated facets emitted  $P \approx 600 \text{ mW}$  from a single facet, corresponding to  $P \approx 1.2 \text{ W}$  for both facets. The slope efficiency of the  $1.0 \text{ mm}$  long device was  $303 \text{ mW A}^{-1}$  at 10 K. Taking into account of the ratio  $\alpha_m/(\alpha_w + \alpha_m)$ , the slope efficiency seems to be larger than expected one of the double metal waveguide device, probably due to the lower collected power by the non-ideal far-field pattern of the double metal waveguide. Emission spectrum of the  $1.0 \text{ mm}$  long device covers the broad spectral range from  $4.6$  to  $5.0 \text{ THz}$  including the target frequency ( $4.74 \text{ THz}$ ) (not shown).  $T_{\text{max}}$  of the  $1.0 \text{ mm}$  long device was  $105 \text{ K}$ .

Finally we fabricated third order distributed feedback (DFB) laser structures [27] for continuous wave (CW) and single mode operation which is required for a local oscillator in a heterodyne spectrometer. To decrease electrical power dissipation, the active region thickness was thinned down to  $9 \text{ }\mu\text{m}$  by wet etching after removing the GaAs substrate. As depicted in figure 4(a), the DFB cavity is designed as a lateral corrugated grating with a square tooth shape and fabricated by standard photolithography and inductively coupled reactive ion etching. The width of the DFB cavity is  $20 \text{ }\mu\text{m}$  and the total length limited by the number of the grating period ( $=19$ ) is  $\approx 800 \text{ }\mu\text{m}$ . Figure 4(b) shows emission spectra measured at 10 K. Due to the low transverse mode selectivity, we observed a few mode emissions from the as-processed devices. To suppress the unwanted modes, a thin Ni film ( $10 \text{ nm}$ ), highly absorptive in the THz region, was deposited on the device surface by a self-aligned method. The thin Ni film cleaned emission spectra since it increases waveguide loss on the absorbing end part of the DFB cavity. Although the procedure yielded a 10% increase in  $J_{\text{th}}$  and a reduced  $P$  as depicted in figure 4(c), we achieved a single mode operation with side mode suppression above  $20 \text{ dB}$ . This technique is thus important to increase a yield of the single mode laser operating at the target frequency. Figure 4 displays (d) far-field laser beam pattern and (e) CW emission spectra of one of the QCLs in the DFBs array. All these measurements were done at  $40 \text{ K}$ . A single hot spot was observed in the angle area of  $30^\circ \times 15^\circ$ . Judging from the far field pattern and the estimated effective index of the DFB cavity ( $= 3.06$ ), the observed laser mode is attributed to the higher band edge third order DFB mode. The laser emission frequency was  $4.745 \text{ THz}$  with an output power of  $0.5 \text{ mW}$ , hitting the target frequency of the neutral atomic oxygen fine structure line. The temperature range of  $40$ – $50 \text{ K}$  with an electrical dissipation of  $1 \text{ W}$  is accessible by a stirling-type cryostat which is useful in space-based observatories. We achieved the highest CW output power of  $0.9 \text{ mW}$  at  $45 \text{ K}$  with an electrical power dissipation

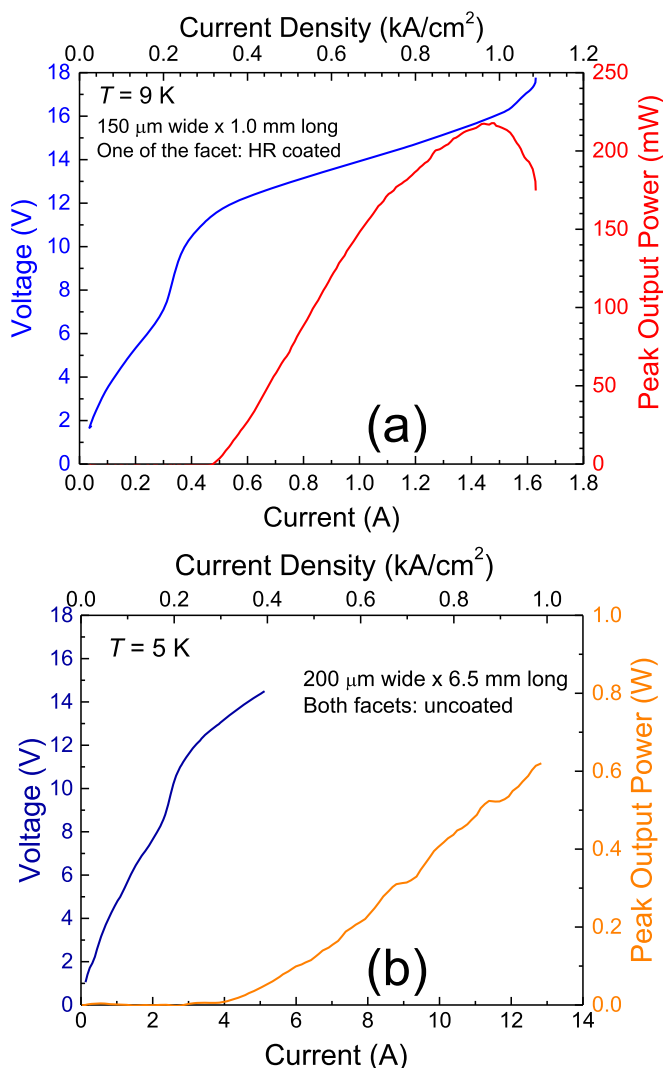


**Figure 3.** Light output–current–voltage characteristics of the single surface plasmon waveguide ridge lasers with (1) 150  $\mu\text{m}$  wide, 1.0 mm long and (b) 200  $\mu\text{m}$  wide, 6.5 mm long device. For the 1.0 mm long device, one of the facets was coated by the  $\text{Al}_2\text{O}_3$  (200 nm)/Au (100 nm) film while both facets left uncoated for the 6.5 mm long one. For 6.5 mm long device, the NDR was not reachable due to limitation of our current pulser.

of 1.2 W at 4.788 THz with the DFB QCLs being cooled in the stirling-type cryostat. The maximum CW operation temperature was 75 K.

The long-term stability of the laser emission frequency is a crucial point for an astronomical heterodyne spectrometer. The laser emission frequency of third order DFB THz QCLs is known to be sensitive to adsorption of molecules on the DFB cavity side wall [28] because of a strong leakage of the optical field by the narrow DFB cavity width; residual gas molecules in the pumped cryostat adsorb and condense on the cavity side wall, leading to a change of the effective index of the waveguide. To avoid it, a small metal cage (shown in figure 5(a)) was used here to trap gas molecules on it. Figures 5(b) and (c) depicts long-term time trace of detector signal from a Michelson interferometer with a fixed mirror position. The pressure inside the cryostat was  $9.0 \times 10^{-8}$  mbar. Without the cage, fringes on the detector signal were visible, revealing presence of a long term frequency drift of the laser frequency. The drift frequency between peaks corresponds to 500 MHz. On the other hand, those fringes were found to disappear with the cage and the long-term laser frequency stability was dramatically improved. This demonstrates that protecting the cavity side wall is important for long-term laser frequency stability of third order DFB THz QCLs. Another issue is a lower beam coupling to a heterodyne mixer device in a heterodyne spectrometer. A waveguide integrated mixer is usually designed to couple to a specific beam pattern such as a Gaussian beam. As shown in figure 4(d), the far-field beam pattern of the third order DFB THz QCL is in a crescent shape, which contains a small portion of the Gaussian beam component, resulting in a lower coupling to the mixer waveguide. A large number of periods of the third order DFB with the perfect phase matching condition [29] should improve it. Other waveguides based on a photonic crystal [30], a patch antenna



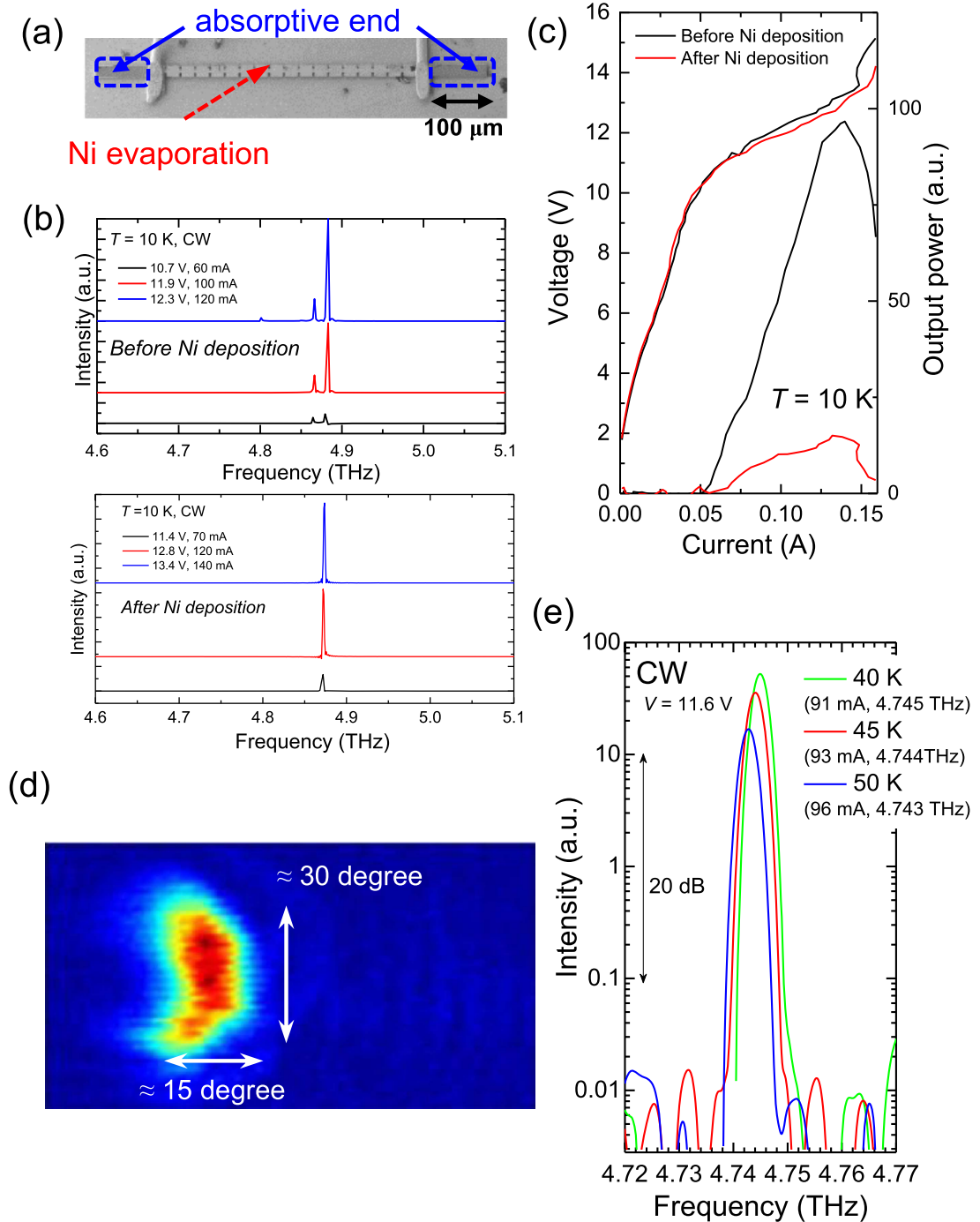


**Figure 4.** (a) Scanning electron microscope image of the fabricated third order distributed feedback THz QCL. To suppress unwanted cavity modes, a thin Ni film was directly deposited on the device surface by a self-aligned method. (b) Emission spectra and (c) light output–current–voltage characteristics before and after the Ni deposition. We found that the thin Ni film cleans emission spectra by increasing the voltage loss on the absorbing end part. A single mode, continuous wave emission spectra (e) at 4.745–4.743 THz and (d) its far-field beam pattern measured at 40 K under the quasi-continuous wave operation.

array [31] and a waveguide integrated block [32, 33] generating a better beam shape could be thus suited, in particular, toward a high power THz local oscillator.

In conclusion, we have studied the characteristics of high frequency GaAs/AlGaAs THz QCL based on the four QW design. The observed  $J_{th}$  and  $J_{max}$  at 10 K were  $200 \text{ A cm}^{-2}$  and  $920 \text{ A cm}^{-2}$ , respectively. The resulting current density dynamic range ( $= 3.6$ ) was about three times larger than the typical 3 THz QCL, leading to  $T_{max} = 150 \text{ K}$  and  $P = 220 \text{ mW}$  at 10 K, which is among the best laser performance at the high frequency THz region. It shows that a large current density dynamic range improves the laser performance of THz QCL. We also demonstrated a 4.74 THz single mode, CW, third order DFB QCLs with a narrow far-field beam pattern (beam divergence of  $30^\circ \times 15^\circ$ ) and a low electrical dissipation (0.8 W) for use as a local oscillator in a

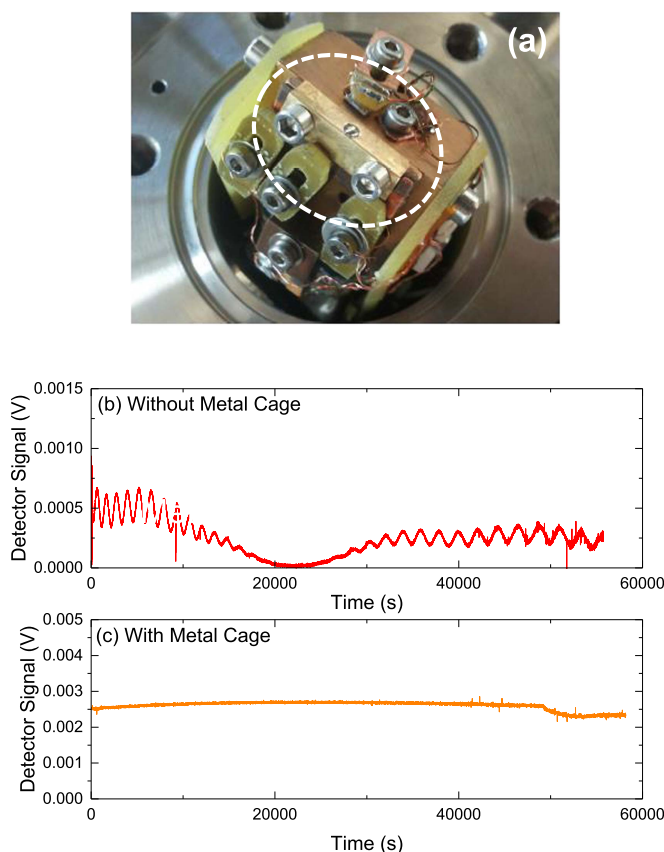


**Figure 5.** (a) Photograph of the mounted third order THz DFB QCL with the metal cage. The metal cage to avoid condensation of gas molecules has a 3  $\mu\text{m}$  Mylar window to extract light. Long-term time trace of the detector signal of the Michelson interferometer (b) without and (c) with the metal cage for protecting the cavity side wall. The DFB laser was biased at 100 mA in the CW mode and the heat sink temperature was kept at 46.0 K.

heterodyne spectrometer. The CW operation temperature around 50 K as well as the electrical power dissipation of 1 W is accessible by a stirling-type cryostat which is useful in space-based observatories.

The authors would like to thank Dr Johanna Wolf for helping to compute the gain coefficient of THz QCLs and Dr Martin J Süess for fruitful discussion on waveguide mode control of the 3rd order DFB THz QCL. This work was supported by ETH Zurich with the FIRST cleanroom facility and carried out within the collaborative research center 956 (SFB956), funded by Deutsche Forschungsgemeinschaft (DFG), the ERC project MUSIC, and the NCCR QSIT project.

## References

- [1] Faist J, Capasso F, Sivco D L, Sirtori C, Hutchinson A L and Cho A Y 1994 *Science* **264** 553
- [2] Köhler R, Tredicucci A, Beltram F, Beere H E, Linfield E H, Davies A G, Ritchie D A, Iotti R C and Capasso F 2002 *Nature* **417** 156
- [3] Rochat M, Ajili L, Willenberg H, Faist J, Beere H E, Davies G, Linfield E and Ritchie D A 2002 *Appl. Phys. Lett.* **81** 1381
- [4] Williams B S, Kumar S, Callebaut H, Hu Q and Reno J L 2003 *Appl. Phys. Lett.* **83** 2124
- [5] Darmon J, Tamosiunas V, Fasching G, Kröll J, Unterrainer K, Beck M, Giovannini M, Faist J, Kremser C and Debbage P 2004 *Opt. Express* **12** 1879
- [6] Lee A W M, Williams B S, Kumar S, Hu Q and Reno J L 2006 *IEEE Photonics Technol. Lett.* **18** 1415
- [7] Gao J R *et al* 2005 *Appl. Phys. Lett.* **86** 244104
- [8] Hübers H-W, Pavlov S G, Semenov A D, Köhler R, Mahler L, Tredicucci A, Beere H E, Ritchie D A and Linfield E H 2005 *Opt. Express* **13** 5890
- [9] Tielens A G G M and Hollenbach D 1985 *Astrophys. J.* **291** 722
- [10] Kloosterman J L, Hayton D J, Ren Y, Kao T K, Hovenier J N, Gao J R, Klapwijk T M, Hu Q, Walker C K and Reno J L 2013 *Appl. Phys. Lett.* **102** 011123
- [11] Richter H, Wienold M, Schrottke L, Biermann K, Grahn H T and Hübers H-W 2015 *IEEE Trans. THz Sci. Technol.* **5** 539
- [12] Wienold M, Röben B, Lü X, Rozas G, Schrottke L, Biermann K and Grahn H T 2015 *Appl. Phys. Lett.* **107** 202101
- [13] Chassagneux Y, Wang Q J, Khanna S P, Strupiechonski E, Coudeville J-R, Linfield E H, Davies A G, Capasso F, Belkin M A and Colombelli R 2012 *IEEE Trans. THz Sci. Technol.* **2** 83
- [14] Chan C W I, Hu Q and Reno J L 2012 *Appl. Phys. Lett.* **101** 151108
- [15] Schrottke L, Wienold M, Sharma R, Lü X, Biermann K, Hey R, Tahaoui A, Richter H, Hübers H-W and Grahn H T 2013 *Semicond. Sci. Technol.* **28** 035011
- [16] Williams B S 2007 *Nat. Photon.* **1** 517



- [17] Rochat M, Faist J, Beck M, Oesterle U and Illegems M 1998 *Appl. Phys. Lett.* **73** 3724
- [18] Amanti M, Scalari G, Terazzi R, Fischer M, Beck M, Faist J, Rudra A, Gallo P and Kapon E 2009 *New J. Phys.* **11** 125022
- [19] Sirtori C, Capasso F, Faist J, Hutchinson A, Sivco D and Cho A Y 1998 *IEEE J. Quantum Electron.* **34** 1722
- [20] Kumar S, Chan C W I, Hu Q and Reno J L 2011 *Nat. Phys.* **7** 166
- [21] Lloyd-Hughes J, Delley Y L, Scalari G, Fischer M, Liverini V, Beck M and Faist J 2009 *J. Appl. Phys.* **106** 093104
- [22] Williams B S, Kumar S, Hu Q and Reno J L 2005 *Electron. Lett.* **42** 89
- [23] Sirtori C, Barbieri S and Colombelli R 2013 *Nat. Photon.* **7** 691
- [24] Terazzi R and Faist J 2010 *New J. Phys.* **12** 033045
- [25] Fatholouloumi S, Dupont E, Wasilewski Z R, Chan C W I, Razavipour S G, Laframboise S F, Huang S, Hu Q, Ban D and Liu H C 2013 *J. Appl. Phys.* **113** 113109
- [26] Li L, Chen L, Zhu J, Freeman J, Dean P, Valavanis A, Davies A G and Linfield E H 2014 *Electron. Lett.* **50** 309
- [27] Amanti M I, Fischer M, Scalari G, Beck M and Faist J 2009 *Nat. Photon.* **3** 586
- [28] Turčinková D, Amanti M I, Castellano F, Beck M and Faist J 2013 *Appl. Phys. Lett.* **102** 181113
- [29] Kao T-Y, Hu Q and Reno J L 2012 *Opt. Lett.* **37** 2070
- [30] Xu G, Li L, Isac N, Halioua Y, Davies A G, Linfield E H and Colombelli R 2014 *Appl. Phys. Lett.* **104** 091112
- [31] Bonzon C, Benea Chelms I C, Ohtani K, Geiser M, Beck M and Faist J 2014 *Appl. Phys. Lett.* **104** 161102
- [32] Valavanis A *et al* 2015 *Electron. Lett.* **51** 919
- [33] Justen M, Ohtani K, Turčinková D, Castellano F, Graf U U and Faist J 2015 *Proc. 26th Int. Symp. on Space Terahertz Technology (Cambridge, MA)* pp T2–5